IET Microwaves, Antennas & Propagation

*Research Article*

IET Journals
The Institution of Engineering and Technology

# Unmanned aerial system for antenna measurement and diagnosis: evaluation and testing

ISSN 1751-8725
Received on 19th November 2018
Revised 8th April 2019
Accepted on 20th May 2019
doi: 10.1049/iet-map.2018.6167
www.ietdl.org

*Maria Garcia-Fernandez*[1] ✉, *Yuri Alvarez Lopez*[1], *Fernando Las-Heras Andres*[1]

[1]*Area de Teoria de la Señal y Comunicaciones, Universidad de Oviedo, Edificio Polivalente, Campus Universitario de Gijon, Gijon, Spain*
✉ *E-mail: garciafmaria@uniovi.es*

**Abstract:** This contribution analyses the performance of an unmanned aerial system for antenna measurement (UASAM) for different kinds of measurement scenarios. UASAM is conceived for antenna diagnostics and characterisation at the operational location of the antenna under test (AUT). The system measures the amplitude of the near field radiated by the AUT. Then, these measurements are post-processed using phase retrieval techniques and equivalent currents methods to obtain an electromagnetic model of the AUT. This model can be used for antenna diagnostics and for evaluating the far field pattern. Similar to antenna measurement systems in anechoic chamber, UASAM allows defining different acquisition grids depending on the type of AUT (planar, cylindrical, arc cylindrical), which also influences the flight time. In addition to this, the capability to measure circularly polarised antennas from amplitude-only measurements is presented, discussing the limitations found during the tests, and comparing the results with those from measurements at a spherical range in an anechoic chamber.

## 1 Introduction

Advances in unmanned aerial vehicles (UAVs) technology have resulted in a burgeoning amount of disruptive applications that make use of their capabilities for accessing remote areas, exploration speed, and ease of operation. Earth observation and mapping [1], infrastructure inspection [2], crops monitoring [3], detection of buried improvised explosive devices such as landmines [4], and acting as hotspots for extending wireless networks coverage [5], are just some of the areas where UAVs, commonly known as *drones*, have been successfully introduced.

In the area of telecommunication networks, where the front-end infrastructure can be located in remote access places (e.g. on top of a building or a mountain), additional costs for inspection a reparation task can be derived with respect to the case of such devices located in accessible places. Even more, in the case of the antennas, they are usually placed several meters above ground. Thus, it is clear that UAV-based systems would be of help for monitoring these elements.

Airborne-based systems for antenna measurements were already developed in 1963 using manned aircrafts [6]. In recent years, developments on small, low-cost consumer UAVs, have made possible the use of these platforms for in-situ antenna measurement and testing at a fraction of the cost of those systems based on manned aircrafts. One of the advantages of using airborne-based systems for antenna measurement is that the antenna can be tested in operational conditions, taking into account how the surrounding environment affects its performance (e.g. reflections in nearby buildings). This kind of test cannot be conducted in antenna measurement facilities such as anechoic chambers, where the antenna is characterised alone. Although the technology maturity of airborne-based antenna measurement systems cannot offer the same accuracy as anechoic chamber measurements, the aforementioned possibility of evaluating the influence of the antenna surroundings on its performance is an added feature of special interest for forthcoming 5G communications systems which will rely on multipath and MIMO techniques [7, 8].

Although different UAV-based systems for antenna testing have been developed recently, the majority are based on a radio-frequency transmitter [9–11] or receiver (a power sensor [12, 13] or a compact spectrum analyser [14]) on board the UAV. Signal levels recorded at each position of the UAV flight path are then geo-referred and latter post-processed (e.g. converting spatial coordinates in polar ones) in order to obtain the radiation pattern of the antenna under test (AUT). In the case of electrically large antennas, or low-frequency communications systems, far-field (FF) distance can be located tens or hundreds of metres away from the AUT, so measuring even a single cut of the radiation pattern could become challenging due to the resulting long flight path for antenna measurement in the FF region. Apart from limitations in the flight autonomy of most UAVs (up to 15–20 min), flight regulations over restricted areas (e.g. crowded places) may add additional constraints. For these reasons, UAV-based systems capable of operating in the near-field (NF) region of the AUT have been proposed [15–19], so that the distance from the AUT to the UAV-based antenna measurement system is not greater than several metres, then applying NF–FF transformation techniques to obtain the AUT radiation pattern.

This contribution reviews recent advances in the validation and testing tasks of an unmanned aerial system for antenna measurement (UASAM), capable of working in the NF region of the AUT, extending the aim and scope of the contribution presented at EuCAP 2018 [16]. The system has been experimentally validated up to C band [15], although simulations emulating realistic flight conditions and measurement uncertainties have proven UASAM capability to operate at millimetre-wave frequency bands [17]. The novelties with respect to the state-of-the-art are: (i) evaluation of different measurement grids in the NF region of the AUT, assessing their impact in antenna measurement, and (ii) capability of UASAM for testing circularly polarised antennas based on the independent acquisition of two linear components. For all the tested antennas, fields recovered on the aperture plane of the AUT as well as the radiation pattern will be compared with results from measurements conducted at a spherical range in an anechoic chamber.

## 2 Description of the proposed system

### *2.1 UASAM hardware architecture*

UASAM prototype, depicted in Fig. 1, is composed by the following subsystems:

- Flight control subsystem (Fig. 1, text in green colour), containing the flight controller, the communication devices and the usual positioning sensor on board the majority of small consumer UAVs. These sensors are a barometer, inertial

measurement units (IMUs), and a Global Navigation Satellite System (GNSS) receiver.

- Accurate positioning subsystem (Fig. 1, text in blue colour), consisting of a laser rangefinder and a real-time kinematic (RTK) system. The latter has two elements: one RTK beacon on board the UAV and the other RTK beacon at a fixed position in ground. The ground beacon acts as base station sending GNSS corrections to the rover beacon.
- Antenna measurement subsystem (Fig. 1, text in red colour), which includes a probe antenna and a power sensor.
- Ground control station (e.g. a laptop) where the geo-referred amplitude-only measurements are post-processed.

Fig. 2 shows a scheme of the main components of the UASAM prototype together with the connections between them.

The flight path of the UAV is created using waypoints, taking as input a pre-defined AUT measurement grid: a cylinder, a cylindrical arc, or a plane. It must be indicated that the UAV heading points towards the AUT in the case of cylindrical grids (as in cylindrical measurement ranges), whereas the heading is perpendicular to the AUT aperture plane in the case of planar grids. The UAV coordinates and the measurements of the power detector are sent to the ground station, where they are post-processed to perform antenna diagnostics and to obtain the radiation pattern.

### 2.2 Measurements post-processing

Geo-referred amplitude-only NF measurements need to be processed in order to calculate the AUT radiation pattern as well as to obtain antenna diagnostics information (e.g. detection of malfunctioning elements). NF–FF transformation and antenna diagnostics techniques [20–24] require information of both amplitude and phase of the NF. Thus, phase retrieval techniques from amplitude-only NF measurements have been considered in UASAM.

Phase retrieval techniques can be classified into two main groups. On the one hand, indirect off-axis holography is based on the knowledge of a reference field and an interference pattern with the field radiated by the AUT [25]. Recent advances on indirect off-axis holography allows for independent phase recovery at each measurement point in the case of broadband antennas [26], complemented with scalar calibration techniques [27]. On the other hand, iterative phase retrieval techniques consist of a minimisation of a cost function relating the amplitude of the NF measured on two or more acquisition surfaces, with the amplitude of the NF radiated by an electromagnetic equivalent model of the AUT on such surfaces. This model can be, for example, an equivalent currents distribution or extremely NF on the AUT aperture plane [28–30]. Iterative techniques require less hardware than indirect off-axis holography, but at the expense of longer acquisition and processing time. Also, the ill-conditioning nature of the inverse problem to be solved influences the convergence of the iterative method. Nevertheless, the requirement of cheap, low-cost hardware on board the UAV has conditioned the choice of an iterative phase retrieval technique over off-axis indirect holography.

In the case of UASAM, the phaseless sources reconstruction method (pSRM) for antenna diagnostics and NF–FF transformation [30] has been considered for processing geo-referred NF measurements acquired in two measurement surfaces. A flowchart of this iterative method is shown in Fig. 3, whereas a discussion about how geo-referring uncertainties and positioning errors affect pSRM performance is presented in [15].

### 2.3 Comparison flowchart

To validate the antenna diagnostics and the radiation pattern calculated using UASAM, antennas tested in this contribution have been measured at a spherical range in an anechoic chamber as well. As depicted in Fig. 4, two methodologies for validation of the results are proposed: (i) calculation of aperture fields and FF pattern from complex NF measurements in anechoic chamber (Fig. 4, green path), and (ii) using an equivalent model of the AUT from these NF measurements [22], the amplitude of the NF is

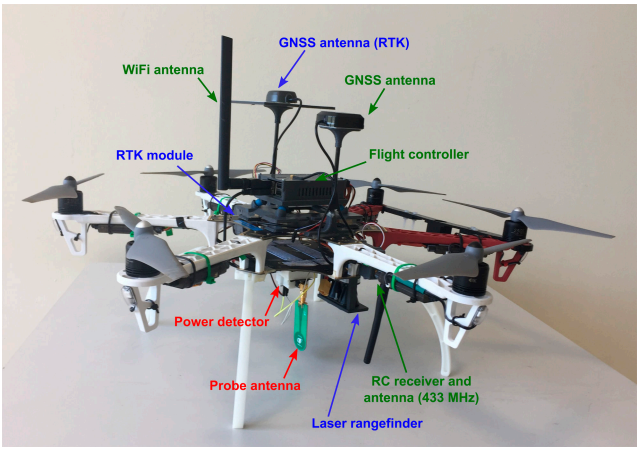


**Fig. 1** *UASAM prototype. Main subsystems are highlighted in different colours: flight control subsystem (green), accurate positioning subsystem (blue), antenna measurement subsystem (red)*

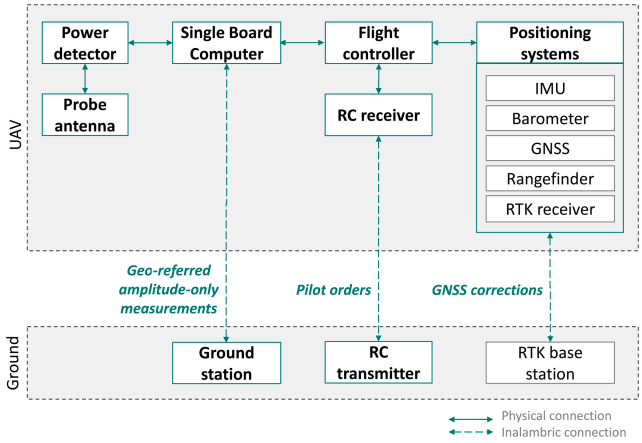


**Fig. 2** *Overview of UASAM architecture: main components and connections between them*

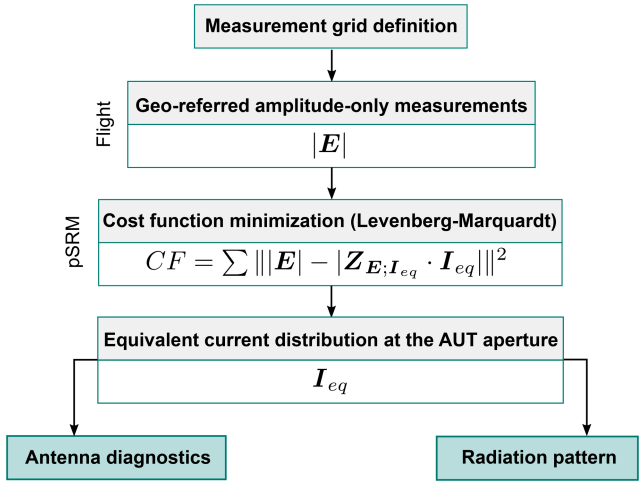


**Fig. 3** *Flowchart of the phaseless sources reconstruction method. $Z_{E;I_{eq}}$ is the impedance matrix relating the radiated field E with an equivalent currents distribution (electric and/or magnetic) $I_{eq}$ that radiates the same fields as the AUT*

calculated at the geo-referred flight path positions of the UAV. Then, these measurements are processed with the pSRM in-situ measurements (Fig. 4, yellow path). The goal is to have an assessment of different sources or error, such as positioning and geo-referring uncertainties, and the nonlinearity of the power sensor.

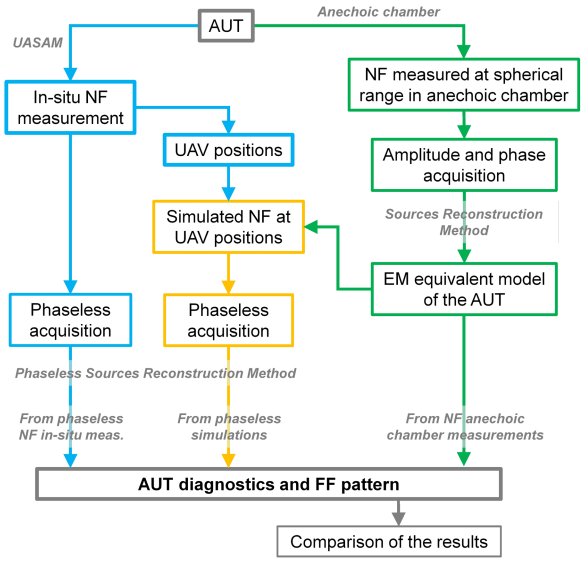


**Fig. 4** *Flowchart of the implemented methodology for comparing measurements accuracy*

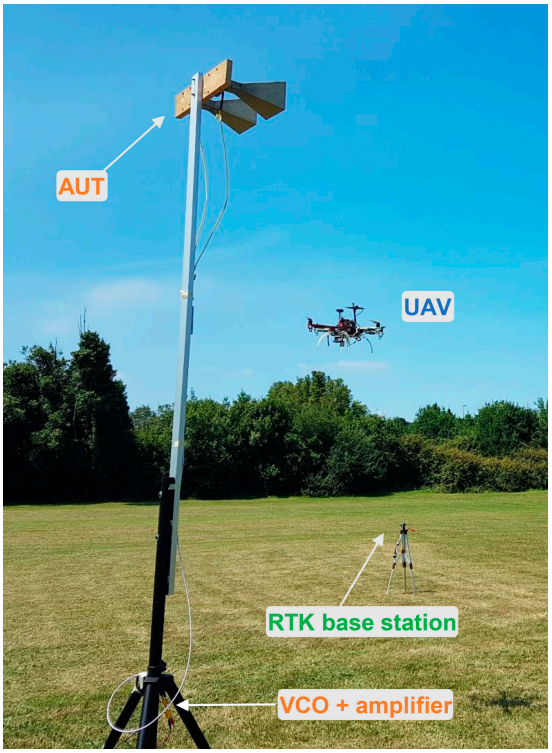


**Fig. 5** *UASAM measurement setup. The AUT is a 2-horn antenna array*

## 3 Evaluation of different measurement grids

In this section, the influence of different acquisition grids in the FF pattern and in the aperture fields of the AUT, is evaluated. For this example, a two horn antenna array working at C band (from 4 to 6 GHz) has been selected as AUT [15]. It is fed with a voltage controller oscillator (VCO) and an RF amplifier which provides a +10 dBm signal at 4.65 GHz. The AUT is fixed to a mast at 3 m height and the distance between the horn aperture centres is approximately 4$\lambda$. The measurement setup is shown in Fig. 5.

Concerning the probe antenna on board the UAV, a commercial printed monopole working from 4 to 7 GHz with vertical polarisation and an omnidirectional pattern in azimuth ($\pm$1.5 dB accuracy) has been chosen [15, 31]. For this example, only the copolar component (vertical polarisation) is measured, which also simplifies the integral equation formulation of the pSRM algorithm [30], as the $x$-component of the equivalent magnetic currents on the

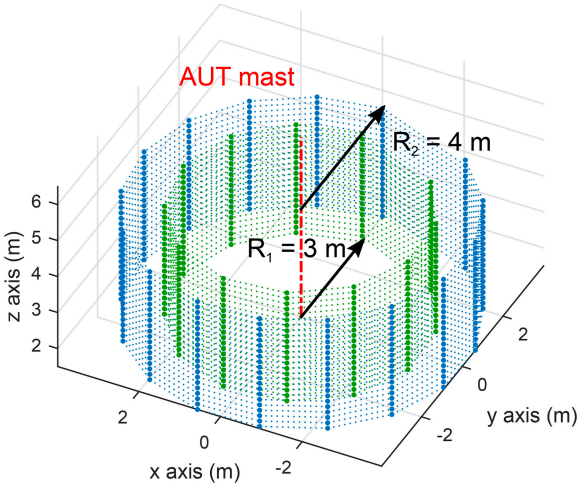


**Fig. 6** *Grid #1: cylindrical grid of radius $R_1 = 3$ m and $R_2 = 4$ m, with the scanning height going from 1.5 to 4.5 m in 0.15 m steps*

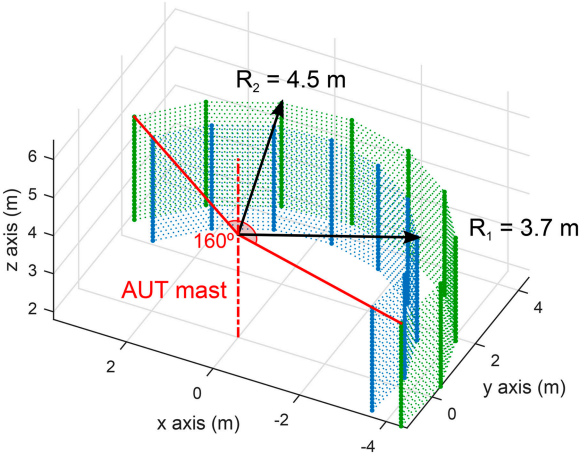


**Fig. 7** *Grid #2: arc cylindrical surfaces of radius $R_1 = 3.7$ m and $R_2 = 4.5$ m, with the scanning height going from 2 to 4.5 m in 0.1 m steps*

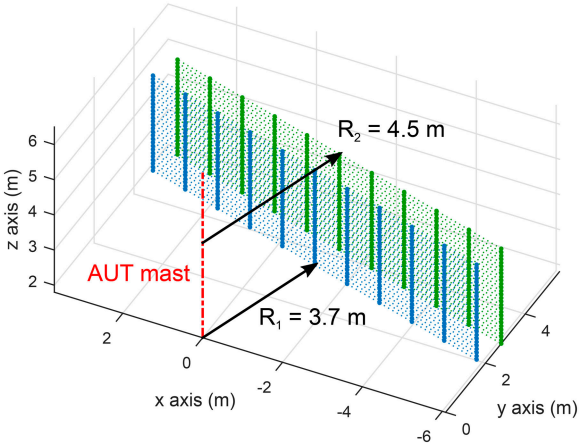


**Fig. 8** *Grid #3: parallel planes of 10 m width at $R_1 = 3.7$ m and $R_2 = 4.5$ m, with the scanning height going from 1.8 to 4.5 m in 0.1 m steps*

AUT aperture plane, $M_x$, is calculated from the measured $z$ (vertical)-component of the NF, $E_z$.

### 3.1 Measurement grids

Measurement grids are defined in a flight plan (composed of waypoints) that the UAV autonomously tries to follow. Cylindrical, arc cylindrical, and planar grids evaluated in this example are depicted in Figs. 6–8. Dashed lines represent the pre-defined flight paths, whereas the waypoints are represented with thick dots. In the

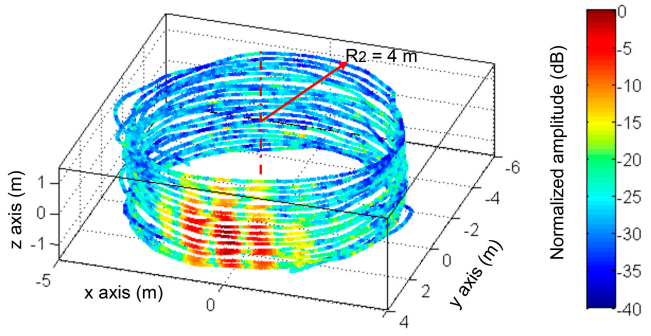


**Fig. 9** *Measured NF amplitude for grid #1 at $R_2 = 4$ m radius*

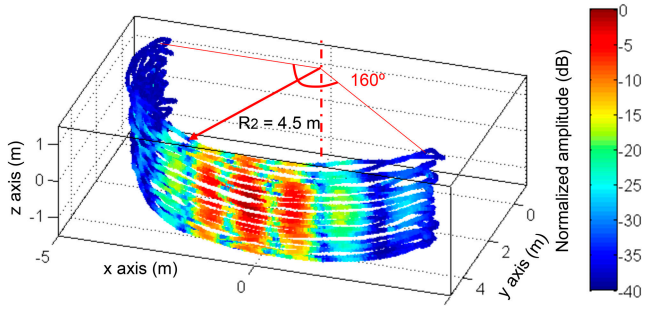


**Fig. 10** *Measured NF amplitude for grid #2 at $R_2 = 4.5$ m radius*

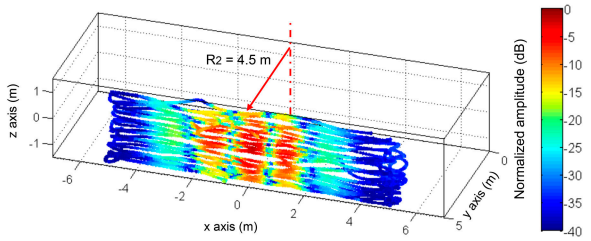


**Fig. 11** *Measured NF amplitude for grid #3 at $R_2 = 4.5$ m*

case of grids #2 and #3, the distance from the AUT has been increased for safety reasons. For the cylindrical grids, the UAV heading points always towards the AUT, whereas in the planar grid the UAV heading is perpendicular to the AUT aperture.

### 3.2 NF measurements

For each tested grid, the amplitude of the measured NF is depicted in Figs. 9–11, where the axes are centred at the AUT position (for the sake of simplicity, only the NF on the surface at distance or radius $R_2$ is shown). AUT – probe antenna misalignment is more noticeable in planar measurement grids (grid #3). In addition, these misalignments increase as the acquisition plane gets closer to the AUT.

The size and geometry of the acquisition grid define the truncation error, which determines the region of the FF pattern that can be calculated from NF measurements (angular region of validity) [20]. Table 1 shows the angular region of validity for the measurement domains considered in this contribution. Most of the grids are limited in the vertical direction, as a trade-off between the limited life of UAV batteries and maximising the angular region of validity in this direction. In the case of amplitude-only NF measurements in two or more measurement surfaces, the angular region of validity is defined by the furthest grid. In the case of spherical NF measurements, there is no truncation error.

Measurement grid geometry also has an impact in the UAV flight time, which in this case is directly the NF acquisition time. For this test, UAV flight times were 25 min for grid #1, 20 min for grid #2, and 17 min for grid #3. In the case of grid #1, flight time would have been even longer if the measurements had been taken at a grid with the same radius as grid #2.

**Table 1** Sizes and FF angular region of validity (ARV) of the measurement domains considered in this contribution (L: horizontal size, V: vertical size)

| Grid (type) | $R_2$ (grid distance) | Grid size | ARV horizontal axis | ARV vertical axis |
|---|---|---|---|---|
| grid #1 (cylindrical) | 4 m | $V = 3$ m | full range | 41° |
| grid #2 (180°-arc cylindrical) | 4.5 m | $V = 2.5$ m | 180° | 30° |
| grid #3 (planar grid) | 4.5 m | $H = 7$ m | 76° | 34° |
| — | — | $V = 2.7$ m | — | — |
| example 2 (planar grid) | 4.5 m | $H = 5$ m | 68° | 31° |
| — | — | $V = 2.5$ m | — | — |

### 3.3 Antenna diagnostics and FF pattern comparison

An equivalent magnetic currents distribution ($M_x$) is reconstructed on the AUT aperture plane, truncated to a rectangular domain of $60 \times 60$ cm. This domain is large enough to contain the projected physical AUT aperture, but not too large to avoid increasing the number of unknowns (i.e. points where the equivalent magnetic currents are recovered).

Reconstructed equivalent currents are depicted in Fig. 12 for the following cases: using complex NF measurements at anechoic chamber (Fig. 12*a*), from simulated NF amplitude at UAV positions for grid #1 (Fig. 12*b*) (cylindrical), and for NF amplitude measurements with UASAM for grids #1 (Fig. 12*c*), #2 (Fig. 12*d*) and #3 (Fig. 12*e*). In all cases, the location and relative power of each element of the horn antenna array can be estimated.

Differences between Figs. 12*a* and *b* are mainly due to the use of amplitude-only NF information in the latter case, and the truncation error of the cylindrical domain in elevation ($z$-axis) of grid #1. In fact, differences are observed along the $z$-axis rather than along the $x$-axis. Next, if Figs. 12*b* and *c* are compared, the effects of geo-referring errors and probe antenna misalignments in the reconstruction quality can be observed.

When the grid is composed of arc cylindrical surfaces, Fig. 12*d*, the reconstruction is slightly worse due to the smaller size of the grid along $z$ yielding greater truncation error (see Table 1) even though the AUT is directive. The fact that the UAV stops at each arc endpoint to change direction also implies that the UAV deviations from the ideal path are slightly increased.

The greatest similarity of reconstructed aperture fields between anechoic chamber measurements and UAV measurements is achieved when a planar grid is considered, as observed in Fig. 12*e*. This might be because the UAV heading does not change (it is always perpendicular to the AUT), whereas in cylindrical grids the UAV heading is continuously changing to point towards the AUT position. However, the use of planar grids requires to accurately determine the NF measurement domain containing most of the radiated power from the AUT, which is typically restricted to the case of quite directive AUTs.

From the recovered equivalent magnetic currents (i.e. aperture fields), the FF pattern can be calculated. FF pattern cut in the $H$-plane of the AUT is represented in Fig. 13. A good agreement between the reference FF pattern and those measured with UASAM can be observed, especially for the main lobes ($\theta \in [-20°, 20°]$). It must be pointed out that the discrepancies are mainly due to the geo-referring errors (which are around 2 cm in the horizontal plane and 1 cm in the vertical direction).

## 4 Measurement of circularly polarised antennas

The capability of UASAM for conducting measurements of circularly polarised antennas is presented in this section. For this goal, there are two possibilities: (i) use of a circularly polarised antenna as probe (or two with reverse handedness if both circular components have to be measured); (ii) use of a linear polarised

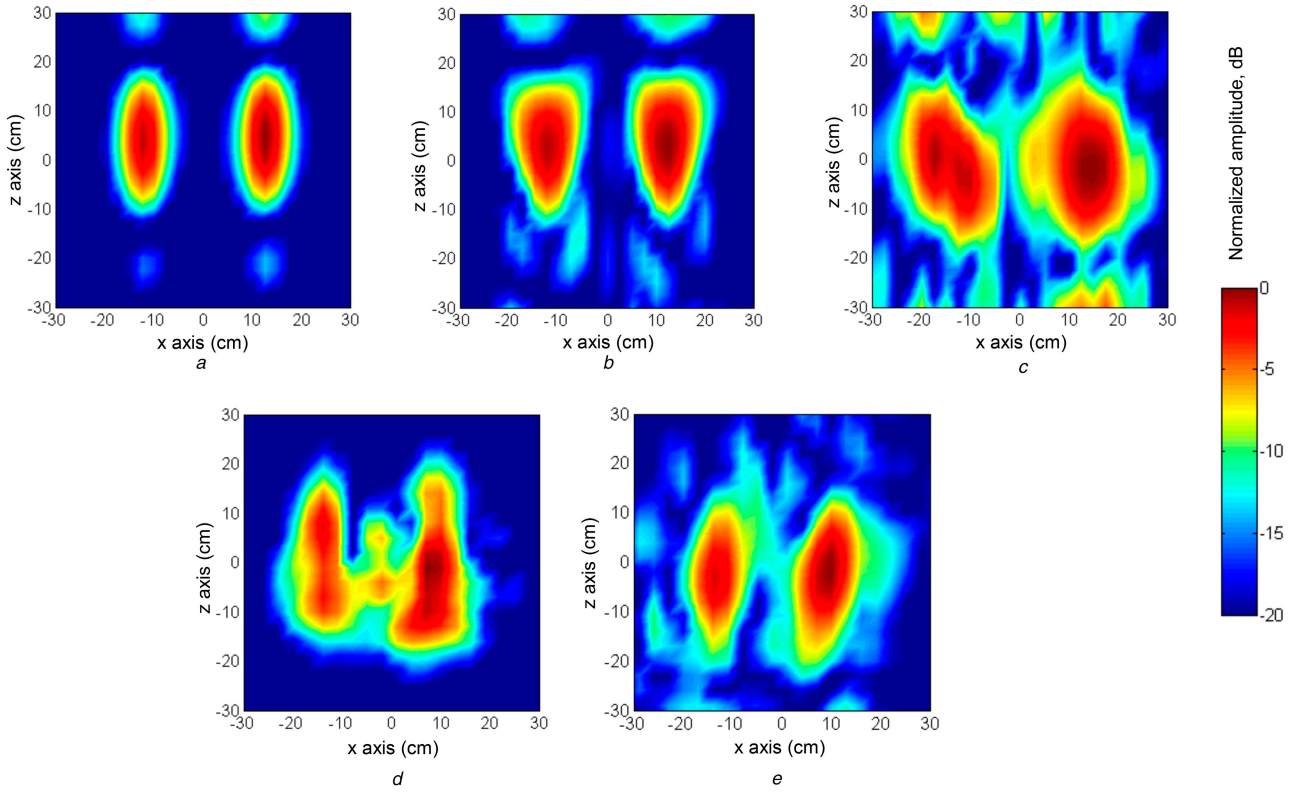


**Fig. 12** *Recovered aperture fields (equivalent magnetic currents distribution, $M_x$) at the AUT aperture*

***(a)*** NF measurements at anechoic chamber, ***(b)*** Simulated NF amplitude at UAV positions for grid #1, ***(c)***, ***(d)***, ***(e)*** NF amplitude measurements with UASAM for grids #1, #2, and #3, respectively

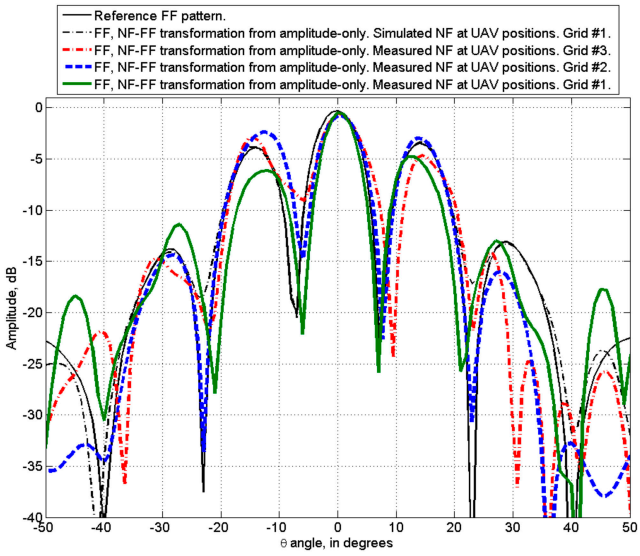


**Fig. 13** *FF patterns obtained from the retrieved equivalent currents (H-plane, $\phi = 0°$). For this cut, FF angular region of validity ranges from $\theta \in [-36°, 36°]$ for grid #3*

antenna as a probe, and measuring the amplitude of the NF with the probe oriented in two orthogonal directions. The latter methodology is simpler in terms of hardware requirements, as linear polarised probes are cheaper and easier to manufacture.

An array composed of circularly polarised antennas with reverse handedness placed in a 3-m height mast is selected as AUT, fed with a VCO tuned at 4.65 GHz, as in the example of Section 3. The same monopole antenna of the previous example [31] will be used as a probe. The measurement setup and the elements involved are depicted in Fig. 14.

Based on the conclusions extracted from the results presented in Section 3, as well as the moderate directivity of the helix antenna (13 dB at 4.5 GHz), the planar acquisition was considered for measurements with UASAM. Planar grids were located at 3.2 and

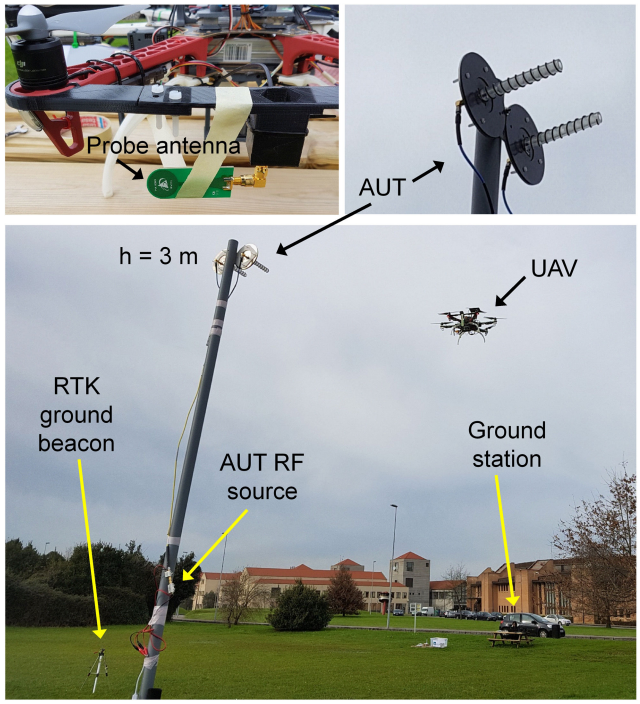


**Fig. 14** *Setup for in-situ measurement of the array of two helix antennas*

4.5 m away from the AUT, with the height ranging from 2 to 4.5 m in 7 cm steps. The calculated FF angular region of validity is indicated in Table 1.

### *4.1 NF measurements*

Two measurements were conducted on each grid, one with the probe parallel to the ground (a measurement of the $|E_x|$ component), and the second with the monopole antenna probe perpendicular to the ground (a measurement of the $|E_z|$ component).

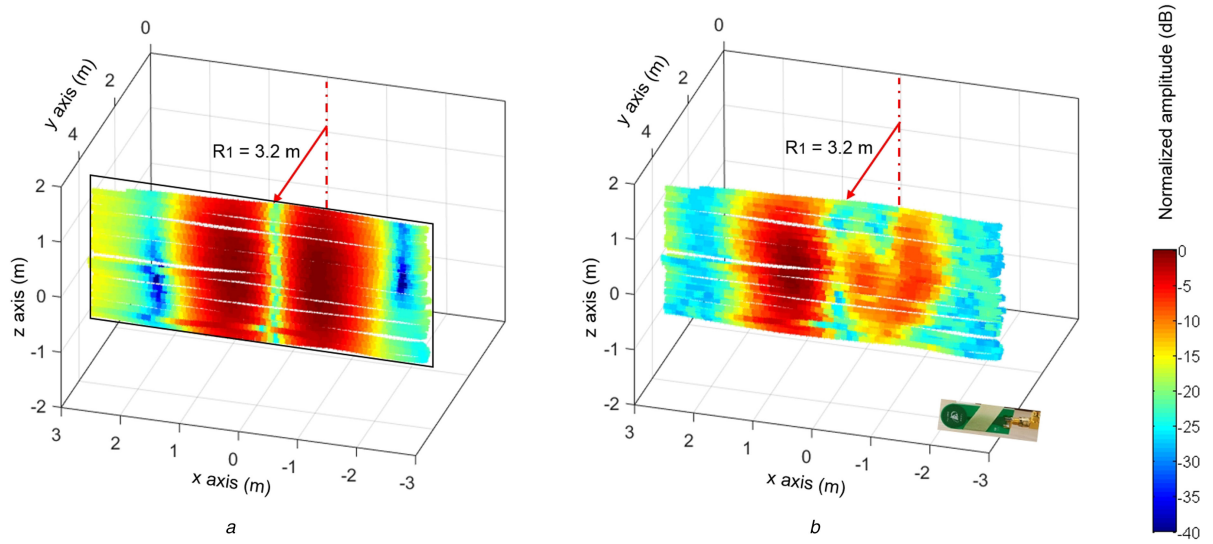


**Fig. 15** *NF of the helix antenna array at the UAV flight path points. Horizontal component (|$E_x$|)*
***(a)*** Evaluated using an EM equivalent model of the AUT, ***(b)*** Measured

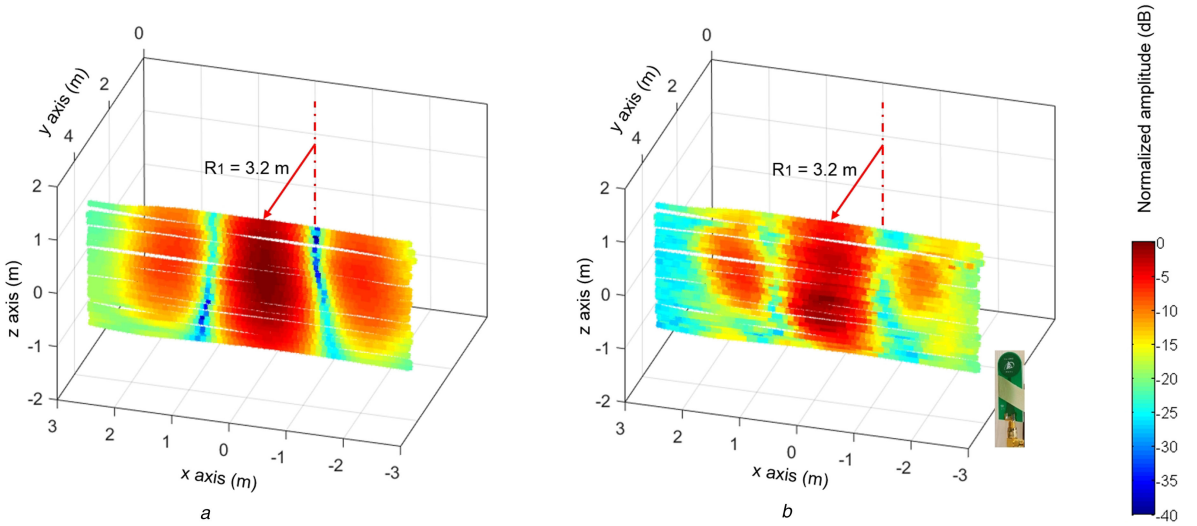


**Fig. 16** *NF of the helix antenna array at the UAV flight path points. Vertical component (|$E_z$|)*
***(a)*** Simulated using an EM equivalent model of the AUT, ***(b)*** Measured

As in Section 3, the AUT was measured at a spherical range in the anechoic chamber, then following the methodology described in Fig. 4 for the comparison of the results.

The amplitude of the NF measured on the planar domain closer to the AUT ($R_1 = 3.2$) is depicted in Figs. 15 and 16 for horizontal (|$E_x$|) and vertical (|$E_z$|) components. Projection of the circularly polarised field onto two orthogonal linear polarisations results in |$E_x$| and |$E_z$| having similar amplitude levels. Next, UASAM measurements are compared with the NF simulated using an electromagnetic equivalent model of the AUT obtained from spherical NF measurements at a spherical range in an anechoic chamber [22]. In the case of the horizontal component, there are some discrepancies between simulations and measurements in the lobe centred at $x = -1$ m, also noticeable in the vertical component (right sidelobe, $x = -2$ m). These differences can be due to multipath contributions, as the electromagnetic model of the AUT obtained from anechoic chamber measurements cannot take into account reflections on the area where the AUT is placed.

It must be mentioned that the limited battery life of the UAV required two different flights for measuring horizontal and vertical components on each acquisition grid (i.e. four flights overall). Even though the same waypoints were uploaded into the UAV flight controller, UAV positioning errors resulted in small differences between the measurement positions for each component, as it can be noticed if comparing positions depicted in Figs. 15 and 16.

### *4.2 Antenna diagnostics and FF pattern comparison*

Amplitude-only NF measurements are introduced in the pSRM to recover an equivalent magnetic currents distribution on the AUT aperture plane. For this measurement setup, the second electromagnetic equivalence principle [21] can be applied, allowing decoupling the integral equations relating the two orthogonal components of the NF ($E_x, E_z$) with the two orthogonal components of the equivalent magnetic currents on the aperture plane ($M_z, M_x$). These equivalent magnetic currents can be combined to obtain the right- and left-handed circularly polarised components ($M_{\mathrm{RHC}}$ and $M_{\mathrm{LHC}}$).

Reconstructed $M_{\mathrm{RHC}}$ and $M_{\mathrm{LHC}}$ are depicted in Fig. 17, comparing those reconstructed from UASAM measurements with those reconstructed from the simulated NF on the measurement grid. In both cases, the highest amplitude corresponds to the helix antenna that has this polarisation. Note that a null appears at the location of the other helix antenna that has reverse handedness. As in the example of Section 3, geo-referring uncertainties result in worse reconstruction. The displacement in the AUT position comes from the fact that the AUT is centred at different positions in the case of anechoic chamber measurements (Figs. 17*a* and *b*: −5 cm

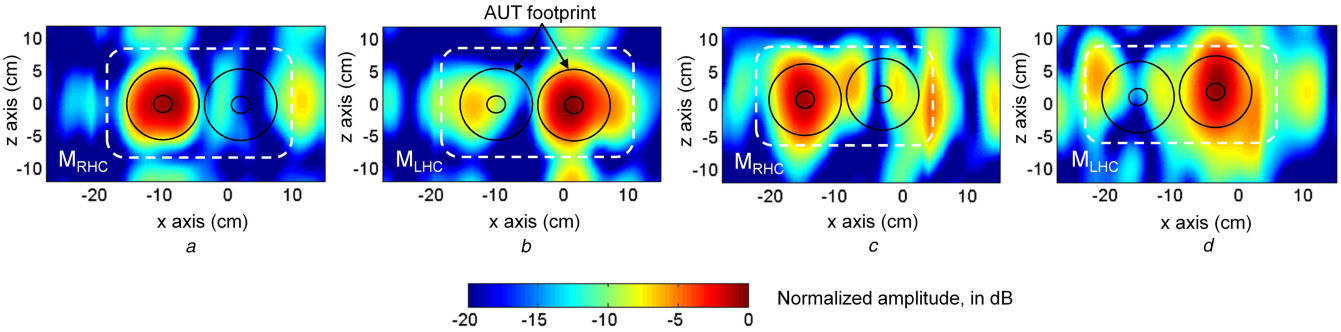


**Fig. 17** *Equivalent currents distribution at the AUT aperture plane, reconstructed from amplitude-only NF acquired in the UAV flight path points*
***(a)***, ***(b)*** From simulated NF, ***(c)***, ***(d)*** From measurements

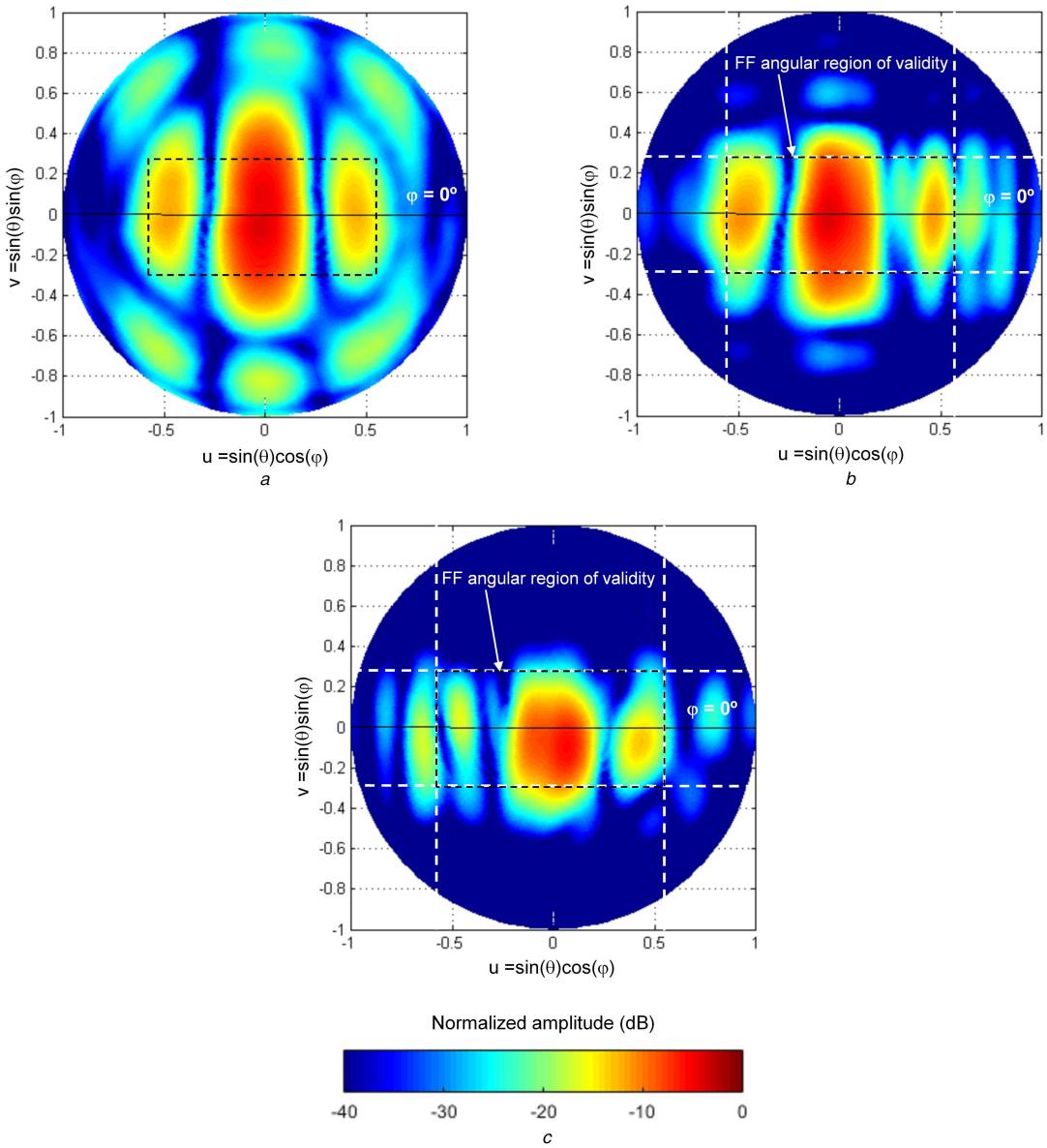


**Fig. 18** *FF patterns ($E_\theta$) obtained from the retrieved equivalent currents*
***(a)*** From complex NF measurements at the spherical range in an anechoic chamber, ***(b)*** From the amplitude of the NF simulated at UAV measurement grids, ***(c)*** From UASAM measurements

offset) and in-situ measurements with UASAM (Figs. 17*c* and *d*: −9 cm offset).

Finally, from the reconstructed equivalent magnetic currents, the FF pattern can be calculated. Only the area of the aperture plane within the dashed white line depicted in Fig. 17 has been considered for calculating the FF pattern, for filtering non-desired contributions to the FF.

Comparison of FF patterns calculated from NF measurements at the anechoic chamber, from simulated amplitude-only NF at UAV acquisition grid, and from UASAM measurements, is shown in Figs. 18 and 19. It can be observed an agreement in the main lobe and the sidelobe centred at $\theta = 30°$. However, there are some discrepancies in the left sidelobe (centred at $\theta = -30°$) which are related to those observed in NF measurements. The effects of the

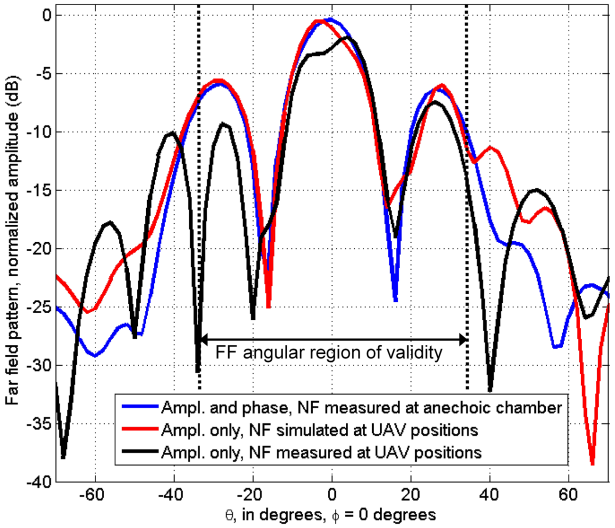


**Fig. 19** *FF patterns ($E_\theta$) obtained from the retrieved equivalent currents. Cut $\phi = 0°$ (plane parallel to the ground)*

truncated NF measurement domain can also be noticed in the results plotted in Fig. 18, especially in the *v*-axis.

## 5 Conclusion

In this contribution, the use of UASAM for measuring antennas in their operational location is analysed. In particular, the performance of different acquisition grids has been tested using a two-element horn antenna array working at C band as AUT. It has been shown that measuring at two complete cylindrical surfaces requires the longest flight time. Truncating it to arc cylindrical surfaces (160°) degrades the quality of the reconstructed equivalent currents distribution but the flight time is not greatly reduced. However, using planar measurement surfaces does not degrade the quality (as compared to cylindrical surfaces) and it takes around 35% less time. In this case, the main challenges are the increase of probe antenna misalignments and the need of defining the size of the planar domain so that most of the power radiated by the AUT is collected, but also taking into account UAV battery life, which influences the size of the measurement domain (defined using waypoints). Based on these conclusions, UASAM capability for circularly polarized antenna measurement has been evaluated, selecting an array of two helix antennas with reverse handedness as AUT. Results proved the capability of recovering both right- and left-handed circularly polarised field components from the independent measurement of two orthogonal components (horizontal and vertical).

## 6 Acknowledgment

This work was partially supported by the 'Ministerio de Economía y Competitividad' of Spain/FEDER under projects TEC2014-55290-JIN (PORTEMVISION) and TEC2014-54005-P (MIRIIEM); by the 'Ministerio of Educación y Cultura' of Spain under FPU grant FPU15/06341; and by of the Government of the Principality of Asturias (PCTI) and European Union (FEDER) under grant IDI/2018/000,191.

## 7 References

[1] Llort, M., Aguasca, A., Martinez, C.L., *et al.*: 'Initial evaluation of SAR capabilities in UAV multicopter platforms', *IEEE J. Sel. Top. Appl. Earth Obs. Remote Sens.*, 2018, **11**, pp. 127–140

[2] Jordan, S., Moore, J., Hovet, S., *et al.*: 'State-of-the-art technologies for UAV inspections', *IET Radar Sonar Navig.*, 2018, **12**, pp. 151–164

[3] Cunliffe, A.M., Brazier, R.E., Anderson, K.: 'Ultra-fine grain landscape-scale quantification of dryland vegetation structure with drone-acquired structure-from-motion photogrammetry', *Remote Sens. Environ.*, 2016, **183**, pp. 129–143

[4] Fernandez, M.G., Lopez, Y.A., Arboleya, A.A., *et al.*: 'Synthetic aperture radar imaging system for landmine detection using a ground penetrating radar on board an unmanned aerial vehicle', *IEEE Access*, 2018, **6**, pp. 2169–3536

[5] Gharibi, M., Boutaba, R., Waslander, S.L.: 'Internet of drones', *IEEE Access*, 2017, **5**, pp. 22166–22176

[6] Barnes, C.: 'Full-scale HF antenna pattern measurements made with transmitter towed by aircraft'. Standford Research Institute, 1963. Research Memorandum 9. Available at http://www.dtic.mil/dtic/tr/fulltext/u2/630092.pdf

[7] Al-Tarifi, M.A., Sharawi, M.S., Shamim, A.: 'Massive MIMO antenna systems for 5G base stations with directive ports ans switched beamsteering capabilities', *IET Microw. Antennas Propag.*, 2018, **12**, pp. 1709–1718

[8] Lee, C., Khattak, M.K., Kahng, S.: 'Wideband 5G beamforming printed array clutched by LTE-A 4 × 4 multiple-input-multiple-output antennas with high isolation', *IET Microw. Antennas Propag.*, 2018, **12**, pp. 1407–1413

[9] Virone, G., Lingua, A.M., Piras, M., *et al.*: 'Antenna pattern verification system based on a micro unmanned aerial vehicle (UAV)', *IEEE Antennas Wirel. Propag. Lett.*, 2014, **13**, pp. 169–172

[10] Paonessa, F., Virone, G., Addamo, G., *et al.*: 'UAV-based pattern measurement of the SKALA'. Proc. of the IEEE Int. Symp. on Antennas and Propagation (APSURSI), Vancouver, BC, Canada, July 2015, pp. 1372–1373

[11] Chang, C., Monstein, C., Refregier, A., *et al.*: 'Beam calibration of radio telescopes with drones', *Publ. Astron. Soc. Pac.*, 2015, **127**, pp. 1131–1143

[12] Sharawi, M.S.: 'Unmanned aerial vehicle for antenna radiation characterization'. WIPO Patentscope, 2016, patent US20160088498A1. Available at https://patents.google.com/patent/US20160088498A1/en

[13] Teng, E., Falcao, J.D., Dominguez, C.R., *et al.*: 'Aerial sensing and characterization of three-dimensional RF fields'. 2nd Int. Workshop on Robotic Sensor Networks, Seattle, WA, USA, April 2015, pp. 1–6

[14] Schreiber, J.: 'Antenna pattern reconstitution using unmanned aerial vehicles (UAVs)'. IEEE Conf. on Antenna Measurements and Applications (CAMA), Syracuse, NY, USA, October 2016, pp. 1–3

[15] Fernandez, M.G., Lopez, Y.A., Arboleya, A., *et al.*: 'Antenna diagnostics and characterization using unmanned aerial vehicles', *IEEE Access*, 2017, **5**, pp. 23563–23575

[16] Fernandez, M.G., Alvarez, Y., Heras, F.L.: 'Evaluation of an unmanned aerial system for antenna diagnostics and characterization'. 2018 European Conf. on Antennas and Propagation (EuCAP), London, UK, April 2018, pp. 1–5

[17] Fernandez, M.G., Lopez, Y.A., Heras, F.L.: 'On the use of unmanned aerial vehicles for antennas and coverage diagnostics in mobile networks', *IEEE Commun. Mag.*, 2018, **5**, pp. 72–78

[18] Bolli, P., Pupillo, G., Paonessa, F., *et al.*: 'Near-field experimental verification of the EM models for the LOFAR radio telescope', *IEEE Antennas Wirel. Propag. Lett.*, 2018, **17**, pp. 613–616

[19] Alvarez-Lopez, Y., Garcia-Fernandez, M., Heras, F.L., *et al.*: 'Airborne system and method for the characterization and measurement of antennas or radiating systems'. Espacenet, 2017, patentWO2018158472 (A1). Available at https://patents.google.com/patent/WO2018158472A1/es

[20] Yaghian, A.D.: 'An overview of near-field antenna measurements', *IEEE Trans. Antennas Propag.*, 1986, **34**, pp. 30–45

[21] Petre, P., Sarkar, T.K.: 'Planar near-field to far-field transformation using an equivalent magnetic current approach', *IEEE Trans. Antennas Propag.*, 1992, **40**, pp. 1348–1356

[22] Alvarez, Y., Heras, F.L., Pino, M.R.: 'Reconstruction of equivalent currents distribution over arbitrary three-dimensional surfaces based on integral equation algorithms', *IEEE Trans. Antennas Propag.*, 2007, **55**, pp. 3460–3468

[23] Araque, J.L., Vecchi, G.: 'Improved-accuracy source reconstruction on arbitrary 3-D surfaces', *IEEE Antennas Wirel. Propag. Lett.*, 2009, **8**, pp. 1046–1049

[24] Saccardi, F., Mioc, F., Iversen, P.O., *et al.*: 'Application of the TSWE algorithm to echo reduction of under-sampled offset spherical near-field measurements', *IET Microw. Antennas Propag.*, 2018, **12**, pp. 549–553

[25] Laviada, J., Arboleya, A., Garcia, C., *et al.*: 'Phaseless antenna diagnostics based on off-axis holography with synthetic reference wave', *IEEE Antennas Wirel. Propag. Lett.*, 2014, **13**, pp. 43–46

[26] Arboleya, A., Laviada, J., Laurinaho, J.A., *et al.*: 'Phaseless characterization of broadband antennas', *IEEE Trans. Antennas Propag.*, 2016, **64**, pp. 484–495

[27] Laviada, J., Arboleya, A., Heras, F.L.: 'Scalar calibration for broadband phaseless antenna measurements based on indirect off-axis holography', *IEEE Trans. Antennas Propag.*, 2018, **66**, pp. 3241–3246

[28] Bucci, O.M., D'Elia, G., Leone, G., *et al.*: 'Far-field pattern determination from the near-field amplitude on two surfaces', *IEEE Trans. Antennas Propag.*, 1990, **38**, pp. 1772–1779

[29] Razavi, S.F., Samii, Y.R.: 'A new look at phaseless planar near-field measurements: limitations, simulations, measurements, and a hybrid solution', *IEEE Antennas Propag. Mag.*, 2007, **49**, pp. 170–178

[30] Alvarez, Y., Heras, F.L., Pino, M.R.: 'The sources reconstruction method for amplitude-only field measurements', *IEEE Trans. Antennas Propag.*, 2010, **58**, pp. 2776–2781

[31] TimeDomain: 'Broadspec UWB antenna datasheet of time domain', 2017. Available at http://www.timedomain.com/datasheets/TD